Preprint version. This manuscript is currently under review.

Title

Core Formation and Geophysical Properties of Mars

Authors

Matthew C. Brennan*[1], Rebecca A. Fischer[1], Jessica C. E. Irving[2]

[1]Harvard University, Department of Earth and Planetary Sciences

[2]Princeton University, Department of Geosciences

*Corresponding author contact: 20 Oxford St, Cambridge MA 02138.

(617) 998-1514

mcbrennan@g.harvard.edu

Keywords

Mars, core formation, Fe–S alloys, Martian core, InSight

Abstract

The chemical and physical properties of the interiors of terrestrial planets are largely determined during their formation and differentiation. Modeling a planet's formation provides important insights into the properties of its core and mantle, and conversely, knowledge of those properties may constrain formational narratives. Here, we present a multi-stage model of Martian core formation in which we calculate core–mantle equilibration using parameterizations from high pressure–temperature metal–silicate partitioning experiments. We account for changing core–mantle boundary (CMB) conditions, composition-dependent partitioning, and partial equilibration of metal and silicate, and we evolve oxygen fugacity (fO_2) self-consistently. The model successfully reproduces published meteorite-based estimates of the bulk silicate Mars composition. This composition implies that the primordial material that formed Mars was significantly more oxidized (0.7–1.4 log units below the iron–wüstite buffer) than that of the Earth, and that core–mantle equilibration in Mars occurred at 45–91% of the evolving CMB pressure. On average, at least 85% of accreted metal and at least 30% of the mantle were equilibrated in each impact, a significantly higher degree of metal equilibration than previously

reported for the Earth. The modeled Martian core is rich in sulfur (16–20 wt%), with less than one weight percent O and negligible Si.

We have used these core and mantle compositions to produce physical models of the present-day Martian interior and evaluate the sensitivity of core radius to crustal thickness, mantle temperature, core composition, core temperature, and density of the core alloy. Trade-offs in how these properties affect observable physical parameters like planetary mass, radius, moment of inertia, and tidal Love number k_2 define a range of likely core radii: 1620–1820 km. Seismic velocity profiles for several combinations of model parameters have been used to predict seismic body-wave travel times and planetary normal mode frequencies. These results may be compared to forthcoming Martian seismic data to further constrain core formation conditions and geophysical properties.

1. Introduction

In the absence of extensive seismic observations like those made available on Earth, our knowledge of the Martian interior relies largely on interpreting measurable geophysical properties, such as mass, radius, moment of inertia, and tidal responses, to constrain the depths, densities, and compositions of the rocky and metallic layers of the planet. While the ongoing InSight mission may directly measure the seismic properties of the interior (Panning et al., 2017), interpreting these data will require an understanding of the Martian composition.

The most detailed information about the chemistry of the Martian interior comes from extrapolating the compositions of the Martian meteorites, particularly the Shergotty-Nakhla-Chassigny (SNC) group, back to their mantle source. Dreibus and Wänke (1985) developed a canonical model for the silicate Mars (updated by Taylor, 2013) by measuring SNC elemental abundances and proposing that their ratios reflect a mixture of volatile-rich and volatile-poor source material. In later studies, such as those of Lodders and Fegley (1997) and Sanloup (1999), compositional models were constructed by matching the oxygen isotopic composition of the SNCs to mixtures of known meteorite types. From these studies, Mars is interpreted to have a mantle enriched in iron oxide (FeO) and a smaller core mass fraction relative to Earth, indicating more oxidizing formational conditions (e.g., Rubie et al., 2011). The proximity of Mars to the protoplanetary snow line during its formation may have resulted in accretion of a larger portion of relatively oxidized, volatile-rich material. Mars is also thought to have a core enriched in sulfur, based on mass balance arguments (e.g., Anderson, 1972) and chalcophile element depletions (Wänke and Dreibus, 1988). Addition of sulfur to iron significantly decreases its melting temperature, so a high S content may have prevented crystallization of an inner core, consistent with the lack of a modern geodynamo on Mars (Williams and Nimmo, 2004; Helffrich 2017).

One difficulty in evaluating the extant compositional models is determining whether they accurately reflect the behavior of planetary materials during core formation. Single-stage core formation models use metal–silicate partitioning data to determine a single pressure–temperature–oxygen fugacity (P–T–fO_2) condition that can simultaneously reproduce the Martian mantle abundances of several elements (e.g., Rai and van Westrenen, 2013; Righter and Chabot, 2011; Steenstra and van Westrenen, 2018), but these models do not account for changing conditions during planetary growth. Rubie et al. (2015) calculated Martian core formation in a multi-stage model with self-consistent fO_2 evolution, though their model did not include S and only used the Martian FeO content (in addition to Earth's mantle composition) as a constraint.

The core formation process on Mars has implications for the modern-day physical state of the planet's interior. Previous studies developed models of the Martian interior that match geophysical parameters such as the bulk density and moment of inertia factor (MOI), and geochemical properties inferred from the SNC meteorites. Sohl and Spohn (1997) developed one model that matched the MOI and another that matched the Fe/Si ratio of Mars. These models improved on earlier assessments by using equations of state to calculate the behavior of Martian minerals at high pressure and temperature and constrained the core size to 1400–1700 km. Bertka and Fei (1998) found a core size compatible with the range of Sohl and Spohn (1997) for Fe–14wt%S (~1400 km). Later measurements of the MOI of Mars, its tidal Love number (k_2), and tidal dissipation factor (Q) seemed to only be matched by models with larger cores. For example, Rivoldini et al. (2011) found that MOI and k_2 were best matched by cores 1730–1860 km in radius. Varying parameters such as the density of the core and the thermal structure of the mantle can produce models that match these same constraints at a range of core sizes (Nimmo and Faul, 2013), so it is important to evaluate the influence of these parameters. Khan et al. (2018) inverted for the most likely ranges of several properties, including core composition, core–mantle boundary (CMB) temperature, and lithospheric thickness, and they constructed seismic velocity profiles based on these ranges. These results also suggest a large core (1730–1840 km), though their Bayesian method does not explicitly consider the influence of each parameter on the determined core size. Larger cores necessarily have more moderate lowermost mantle pressures, probably precluding a region of bridgmanite stability, though Bertka and Fei (1997) determined that the existence of Martian bridgmanite is also highly temperature dependent.

Here we present a new model of Martian core formation, which improves upon previous studies by implementing multi-stage differentiation with comparisons to a large suite of major, minor, and trace elements in Mars. The core and mantle compositions predicted by this core formation model were used to construct mineralogical, density, and seismic velocity profiles for the Martian interior. We explicitly considered how planetary structure is influenced by core composition as well as geophysical parameters such as crustal thickness and thermal structure. Additionally, we introduced more realistic calculations of liquid Fe–S alloy densities at high pressures and temperatures, improving our understanding of the core's physical properties. Seismic properties were assessed across the model suite, allowing predictions of both the body wave travel times and normal mode oscillation frequencies for the different models. The new self-consistent models of core formation, internal structure, and seismic properties presented here help tie together the history of early Mars with its modern state and produce geophysical predictions that can be compared to seismic results obtained by the InSight mission.

2. Methods

We have constructed a model of multi-stage core formation to investigate Martian formational properties and a model of planetary physical structure to investigate geophysical properties of modern Mars. Further details on each of these, as well as a description of our seismological calculations, can be found in the supplementary materials.

2.1 Core formation

Chondritic primordial material was equilibrated at a fixed fO_2 to form planetesimals, then these planetesimals were sequentially added to the proto-Mars, and experimentally-determined metal–silicate partitioning data (Supplementary Table S1) were used to model the chemistry of core formation. The composition of the primordial material was based on CI chondrites (after Dreibus and Wänke, 1985; Taylor, 2013), enhanced in refectory elements (Mg, Al, Si, Ca, V, Cr, Fe, Co, Ni, W, Ti) by a factor of 1.9 (Taylor, 2013) to create relative depletions in moderately volatile elements (Na, P, S, K, Mn). Mars was constructed from 1,000 Ceres-sized (0.001 M_{Mars}) planetesimals.

In each accretionary step, one planetesimal (the impactor) was equilibrated with the proto-Mars (the target). Equilibration took place between the entire impactor mantle, a portion of the impactor core, and a portion of the target mantle; the core of the proto-Mars was assumed to be undisturbed by impacts. In each step, metal–silicate equilibration took place at a constant fraction of the growing CMB pressure and at the liquidus temperature. Pressure at the CMB was increased linearly from 1 GPa to 20 GPa (Rivoldini, 2011). Mg, Al, Ca, Na, K, and P were assumed to be perfectly lithophile. In each step, major elements Si, Fe, O, and Ni were partitioned first, allowing fO_2 to evolve self-consistently following the methodology of Rubie et al. (2011) as updated in Fischer et al. (2017), then trace elements and S were partitioned. Finally, the unequilibrated portion of the impactor core and the metallic portion of the equilibrated material were added to the proto-Martian core, and the unequilibrated portion of the target mantle and the silicate portion of the equilibrated material were combined to form the proto-Martian mantle. This procedure was repeated for each impacting planetesimal.

Adjustable parameters in the model include: the equilibration fraction (the portion that participates in the metal–silicate reaction) of the impactor core (denoted *k*) and target mantle; depth of equilibration, expressed as a fraction of the evolving CMB pressure (denoted P_{equil}/P_{CMB}); and the initial oxidation state of accreted material. To evaluate the sensitivity of the resulting core and mantle compositions to these formational parameters and to constrain them, the equilibration fractions of the impactor core and target mantle were each varied in the range 0.1–1.0, the depth of equilibration was varied in the range 0.01–1.0, and the initial fO_2 of the accreted material was varied from IW–3 to IW. Uncertainties were evaluated using a Monte Carlo analysis.

2.2 Physical structure

Using the core and mantle compositions calculated in the core formation model, radial profiles of density and seismic wave speeds were constructed. The Martian temperature profile (the "aerotherm") was calculated based on an adiabat from the median CMB conditions of Rivoldini et al. (2011) (~20 GPa and ~2000 K). These conditions correspond to a mantle potential temperature of 1600 K, consistent with previous estimates (e.g., Nimmo and Faul, 2013; Zheng et al., 2015). The lithospheric thermal boundary layer was approximated as a layer of linearly increasing temperature which intersects the adiabat at ~200 km, the estimated base of the thermal boundary (e.g., Khan et al., 2018).

The Martian core was assumed to be a homogenous liquid alloy in the Fe–S system, with the S fraction specified by the core formation model. Density–pressure relationships for the core were calculated by reference to published equations of state for Fe–S alloys. The core S content is a function of the formational parameters discussed above, so it was necessary to interpolate between equations of state for several alloys to calculate densities over a range of compositions. We used four equations of state: γ-Fe (Komabayashi and Fei, 2010), Fe_3S (Seagle et al., 2006), FeS (Urakawa et al., 2007), and FeS_2 (Thompson et al., 2016). These equations of state all describe solids, so it was necessary to correct for the difference in density between these and liquid alloys. While it would have been more straightforward to use liquid equations of state, there are not enough data to adequately constrain liquid Fe–S alloy densities over a range of compositions (Section 4.4). Each constructed density and velocity profile of Mars corresponds to a specific set of physical (crust thickness, mantle temperature, core temperature, volume change (ΔV) of melting of Fe–S alloys) and formational (initial fO_2, volatile loss, equilibration depth, degree of equilibration) parameters. To test the sensitivity of core radius and density/velocity structure to these parameters, crust thickness was varied in the range 25–85 km, mantle potential temperature was varied in the range 1500–1800 K, the temperature contrast across the CMB was taken to be 0–600 K, and ΔV of melting was taken to be 2–5%. Each combination of parameters implies a value for the MOI and k_2, which can be compared to the values measured by Mars-orbiting satellites (Konopliv et al., 2011, 2016) (Section 4.4).

3. Martian core formation

The composition of the Martian mantle, as inferred from SNC meteorites, can be used to constrain the conditions of core formation. The core formation conditions implied by the mantle composition can then be used to place constraints on the composition of the core.

3.1 Mantle composition and implications for the formation of Mars

An example of a Martian mantle composition produced by this model is shown in Figure 1. Of the previous studies on Martian mantle composition, we primarily compare our results to those of Taylor (2013) due to that study's reporting of uncertainties, which other studies lack (e.g. Dreibus and Wänke, 1985; Lodders and Fegley, 1996; Sanloup, 1999). The composition predicted by this study best matches those of Taylor (2013) (Figure 1) and Dreibus and Wänke (1985) due to use of the same bulk composition (Section 2.1). We obtain good agreement with Lodders and Fegley (1996) and Sanloup (1999) when we instead use their bulk compositions. Within uncertainty, calculated mantle abundances of most major, minor, and trace elements are consistent with those of Taylor (2013), except for Cr and K (Figure 1). The anomalously low concentration of Cr might arise because we are extrapolating beyond the fO_2 conditions of the metal–silicate partitioning experiments. Taylor (2013) obtained the mantle K abundance from gamma ray spectroscopy measurements of the surface K/Th ratio; this difference in methodology likely accounts for the discrepancy in K. To constrain conditions of the formation and differentiation of Mars, first the fO_2 at which the primordial material equilibrated was adjusted to match the reported FeO content of the Martian mantle. The mantle FeO content implies that Mars was built of material with an initial oxidation of state of IW–1.4 to IW–0.7, which corresponds to a core mass fraction for Mars of 0.18–0.27 (Figure 2a). This higher fO_2 and relatively smaller core than Earth (e.g., Rubie et al., 2011, 2015; Fischer et al., 2017) reflects the accretion by Mars of relatively oxidized primordial material, which likely originated further from the Sun.

Constraints on the degree of equilibration were obtained by comparing the calculated mantle compositions with literature values, as shown in Figure 3a. Possible values of *k* are found to be 0.84–1.0 for whole-mantle equilibration, based on matching the mantle abundances of TiO_2, S, and Co; other elements are consistent with this range but do not provide such tight constraints. This degree of metal equilibration is significantly higher than that found for Earth by examining the variation of mantle trace elements and the Hf–W isotopic system, which imply that k for Earth is 0.2–0.55 (e.g., Fischer and Nimmo, 2018; Fischer et al., 2017). A lower *k* for Earth is consistent with the accretion of giant differentiated impactors, whose large cores would not have efficiently emulsified. Mars' high *k* is consistent with the accretion of smaller impactors, possibly including undifferentiated ones that would exhibit $k \sim 1$. Varying the equilibration fraction of the target silicate does not significantly change the mantle composition for values above ~0.3, consistent with its limited effect on composition above a certain threshold for the Earth (Fischer et al., 2017). Reducing the degree of silicate equilibration requires a corresponding increase in k; since k is already near unity (its maximum value) for the case of whole-mantle equilibration, it is more likely that silicate equilibration was similarly high.

An analogous procedure was used to constrain the depth of metal–silicate equilibration (Figure 3b). Simultaneously matching the Martian mantle abundances of Ni, Co, and S requires that P_{equil}/P_{CMB} fall in the range 0.40–0.91 (for k = 0.9 and whole-mantle equilibration); again, other elements are consistent with this range, but do not further constrain it. This pressure range implies that, on average, equilibration took place in a deep magma ocean but not as deep as the core–mantle boundary. It overlaps with the relative depth of equilibration found for the Earth using similar models (Fischer et al., 2017; Rubie et al., 2011, 2015), which may suggest a similar relative depth of melting on the two planets. Applying this range to the modern Martian CMB implies an average equilibration pressure of ~13 GPa, similar to the results of single-stage partitioning studies (e.g., Rai and van Westrenen, 2013; Righter and Chabot, 2011). Single-stage models necessarily partition elements at a fixed fO_2 and do not incorporate changes in pressure and temperature as a planet grows, so the model presented here represents a more realistic approach.

3.2 Light elements in the Martian core

The core formation conditions implied by the Martian mantle composition indicate that S is the dominant light element in the core, consistent with previous studies (e.g., Lodders and Fegley, 1996; Sanloup et al., 1999; Steenstra and van Westrenen, 2018; Taylor, 2013; Wänke and Driebus, 1985). Sulfur is siderophile at the P–T–fO_2 conditions of Martian core formation, with D_S values as high as 600, comparable to D_{Ni} (Fischer et al., 2015). The majority of Martian

S must be in the core, but the mantle abundance also appears to be greater than that of the Earth (e.g., Wang and Becker, 2017), implying that bulk Mars is relatively sulfur-rich. The range of core mass fractions implied by the mantle FeO content, 0.18–0.25 (Section 3.1), is consistent with a range of volatile element depletion factors of 0.28–0.68× CI (Figure 2b). Taylor (2013) argued for a refractory element enrichment of 1.9× CI (equivalent to a volatile element depletion of 0.6× CI) based on a survey of lithophile volatile element abundances in Mars. Enriching Mars in refractory elements by this factor leads to a core S content of 18 wt%, with the uncertainty of the Monte Carlo analysis expanding this to a preferred range of 16–20 wt% (95% confidence interval; Supplementary Table S2). This corresponds to a bulk Mars with 4.2 wt% S, within the bulk abundance estimates of Steenstra and van Westrenen (2018). If Mars instead is assumed to have bulk S equivalent to an H chondrite, it would have a core S content of 12 wt%. Bulk S content equivalent to a pristine EH chondrite results in a core S content of 21 wt%; this may be taken as the upper limit for core S in a chondritic Mars since EH is the most S-rich of all chondrite groups (Lodders and Fegley, 1998).

The Martian core contains little O (<1 wt%; Supplementary Table S2) despite the more oxidizing core formation conditions compared to the Earth. This is largely due to the less extreme conditions of metal–silicate equilibration on Mars, since O partitions more strongly into iron alloys at higher T (e.g., Fischer et al., 2015). Previous studies which predicted O at the few-percent level in the Martian core (e.g., Steenstra and van Westrenen, 2018) calculated partitioning at modern lowermost mantle conditions (inconsistent with our findings; Figure 3b). The other light element considered here, Si, only enters the Martian core at trace levels (Supplementary Table S2). Like O, it is less siderophile at lower temperatures, but it is also less siderophile at higher fO_2 (e.g., Fischer et al., 2015), further reducing its core abundance.

C or H partitioning into the core were not modeled despite suggestions that these may be present in greater-than-trace abundances (e.g., Chi et al., 2014; Zharkov and Gudkova, 2005). There are few constraints on the planetary or mantle abundances of these highly volatile elements, and thus it is difficult to determine their total budgets. Qualitatively, Mars is too small and S-rich to dissolve substantial H in its core, with Clesi et al. (2018) estimating 60 ppm. The solubility of C is also much reduced in S-rich core alloys (Tsuno et al., 2018). For a nominal bulk C content of 1000 ppm, Tsuno et al. (2018) found that a Martian core at IW–1.0 with 16 wt% S would have ~0.5 wt% C; this may be taken as an upper bound for the more S-rich core composition presented here. Better constraining the abundances and partitioning of these highly volatile elements is a target for future studies.

4. Geophysical properties of Mars

The core and mantle compositions predicted by the core formation model were used to construct phase assemblages (Supplementary Figure S1) and produce density and velocity profiles (Figures 4 and 5) of the Martian interior. In addition to composition, these profiles depend on physical properties of the Martian interior. By comparing to the mass, radius, MOI, and k_2, constraints can be placed on some of Mars' geophysical properties. The resulting solution space allows for predictions of core radii and seismic properties.

4.1 The lithospheric boundary layer

The rigid lithosphere at a planet's surface does not participate in mantle convection, so its heat flow is conductive, with temperatures increasing approximately linearly with depth. On Earth, this rapidly increasing temperature leads to high seismic velocities in the conductive lid and a corresponding low-velocity zone (LVZ) in the uppermost adiabatic mantle. Mars is a stagnant lid planet and is inferred to have a laterally variable lithosphere up to 300 km thick (e.g., Grott et al., 2013). This produces a thick thermal boundary layer on a small planet, so the low-velocity effect which confined to a small portion of the Earth's mantle will extend over a sizeable portion of the Martian mantle. As seen in Figure 5, this may be a property of first-order importance for Martian seismology (Section 4.6). Since the magnitude of the decrease is dependent on the thermal structure of the lithosphere, mantle potential temperatures may be inferred by measuring the LVZ's seismological effects (Zheng et al., 2015).

The magnitude of this effect, however, cannot be well-constrained with our current knowledge of Martian temperature and structure. The calculations shown here use an upper mantle thermal boundary layer thickness of 200 km (Khan et al., 2018) and a range of mantle potential temperatures around 1600 K (Nimmo and Faul, 2013). Lithospheric thickness directly influences the size of the LVZ, but also reduces its magnitude, since a deeper thermal boundary would be shallower and closer in slope to the mantle adiabat. Changing the mantle potential temperature at a constant lithospheric thickness likewise requires changing the slope of the lithospheric temperature profile (Supplementary Figure S2). Increasing potential temperature by 100 K for a 200 km lithospheric boundary increases the magnitude of the LVZ by 0.2 km/s for compressional waves and 0.1 km/s for shear waves. These effects may be complicated by lateral variations in lithospheric thickness due to features such as the hemispherical dichotomy and the Tharsis volcanic province.

4.2 Lowermost mantle conditions

There is some disagreement as to whether the Martian mantle contains bridgmanite, the major component of Earth's lower mantle. Some studies find that the *P*–*T* conditions of the lowermost Martian mantle lie within the bridgmanite stability field (e.g., Bertka and Fei, 1998), some do not (e.g., Sohl and Spohn, 1997; Khan and Connolly, 2008; Khan et al., 2018), and several are inconclusive (e.g., Bertka and Fei, 1997; Rivoldini et al., 2011). At a lower mantle temperature of 2000 K, the parameterization of Fei et al (2004) suggests that bridgmanite becomes stable at 22.9 GPa. This CMB pressure corresponds to a core radius of approximately 1500 km; such a core is smaller than any in Figure 4, but it could be produced by, for example, a low S content, a shallow crust, and no CMB thermal boundary layer. Such a small core is difficult to reconcile with geophysical constraints (see Section 4.4). The bridgmanite stability field grows with temperature, so a hot lower mantle might support bridgmanite at slightly lower pressures. At 2500 K, bridgmanite becomes stable at 22.2 GPa, corresponding to a 1570 km core; such temperatures could only be produced by a CMB thermal boundary layer with a large temperature contrast. This would tend to increase the core radius well beyond this size, meaning that it seems unlikely that bridgmanite exists within modern Mars. A bridgmanite layer would affect mantle convection, increase the temperature of the lower mantle, and reduce heat flow from the core, impacting the both the areothem and the contrast across a CMB thermal boundary layer (Bruer et al., 1998; Michel and Forni, 2011). Thus, if a bridgmanite layer does exist, its thickness will strongly constrain mantle temperature (Bertka and Fei, 1997); the possibility of such a layer in Mars' hotter past may have influenced the convective regime of the Martian mantle towards single-plume upwelling (Sohl and Spohn, 1997).

4.3 The crust

The outer layers of a planet have an outsized influence on the planet's MOI due to their large radial distance from the center of gravity. Konopliv et al. (2011) determined the Martian MOI to be 0.3644 ± 0.0005 but found that altering crustal thickness by 25 km changes the MOI by 0.0017. Therefore, uncertainties in crustal structure dominate the inertia-based constraints on models of the Martian interior. Some recent studies use an even tighter bound on MOI (Khan et al, 2018). Determining the average crustal properties pertinent to a spherically-symmetric model is complicated by the fact that the Martian crust contains a significant dichotomy between the northern and southern hemispheres, various volcanic provinces, impact basins, and heterogeneous regolith. Constraints from orbital gravity measurements and surface topography imply that mean crustal thickness must lie within 57 ± 24 km (Wieczorek and Zuber, 2004), with some studies preferring different portions of this range. We find that within a narrow range of crust sizes (55 ± 10 km) the Martian MOI can be matched with a wide range of core sizes (1500–1850 km). Fortunately, InSight measurements are likely to strongly constrain crustal thickness beneath the landing site (Panning et al., 2017), which will allow for tighter constraints on core size.

4.4 Core radius

We have evaluated the effects of five parameters on the core radius of Mars: the thickness of the crust, temperatures of the mantle and core, sulfur content of the core, and densities of liquid Fe–S alloys. All core radii calculated here are consistent with the core mass fraction range determined in the core formation model (Section 3.1; Figure 2).

(1) Thickness of the crust. A thick layer of relatively light crustal material requires a larger core to maintain consistency with the Martian radius and bulk density. Varying the crustal thickness in the range 25–85 km (Wieczorek and Zuber, 2004) corresponds to a change in core radius of 94 km, with thicker crusts corresponding to larger cores. The planet's MOI is very sensitive to crustal parameters, so only a small portion of this range of crust thicknesses is consistent with measurements (Section 4.3).

(2) Temperature of the mantle. Martian internal temperature profiles depend on the thermal history of the planet, its radiogenic heat production, and its convective regime. These features are not well constrained, making temperatures difficult to evaluate. Lowermost mantle temperatures of 1800–2100 K bracket the "hot" and "cold" endmembers of Rivoldini et al. (2011). This range corresponds to mantle potential temperatures of 1500–1800 K, consistent with published estimates (e.g., Nimmo and Faul, 2013). This temperature range corresponds to a change in core radius of 122 km, with larger cores corresponding to hotter mantles.

(3) CMB thermal boundary layer. Previous studies (e.g., Khan et al., 2018) have generally not considered any significant temperature change across the CMB due to the absence of a Martian geodynamo (Williams and Nimmo, 2004). It is possible that the core is hotter than the overlying mantle, leading to a thin region of rapidly increasing temperatures, analogous to Earth's lowermost mantle. We have investigated models with uppermost core temperatures ranging from 0–600 K above the lowermost mantle temperature, within the allowable range of CMB heat flow (see supplementary materials for more details). This range corresponds to a change in core radius of 103 km, with hotter cores being less dense and thus larger.

(4) Sulfur content of the core. Since S is much lighter than Fe, a core with a large S component will have a reduced alloy density, and thus must be larger. Our compositional results (Section 3.2) indicate that to maintain consistency with the inferred mantle composition, the Martian core contains 16–20 wt% S; this range corresponds to 65 km of variability in core size. A core S content of 12–21 wt% encompasses the range of 2.0–5.4 wt% bulk Martian S, corresponding to the

difference between the most S-poor (H) and S-rich (EH) chondrites (Lodders and Fegley, 1998). This range changes core radius by 141 km.

(5) Effect of melting on Fe–S alloy densities. Since the Martian core is thought to be entirely molten (Konopliv et al., 2011), its geophysical parameters must be calculated with reference to liquid Fe–S alloys. Unfortunately, there are few equation of state studies in this liquid system, and the available ones do not generally extend to the relevant P–T conditions. Some previous studies (e.g., Rivoldini et al., 2011; Khan et al., 2018) have attempted to overcome this difficulty by extrapolating the extant liquid data, but this may underestimate the true density (Figure 6). Several equation of state studies have pointed out that the ΔV between solid and liquid Fe–S alloys should be quite small at high pressures, on the order of 1.5% for the Earth's CMB (Seagle et al., 2006) and only slightly greater for Martian CMB conditions. The ambient ΔV is ~16% for FeS (Kaiura and Toguri, 1979), dropping to only ~4–5% at a few GPa (Nishida et al., 2011). For this study, we have chosen to use the interpolation of the solid densities and correct for a melting effect based on the eutectic melting curve of Fe–S alloys (Campbell et al., 2008), leading to a 3.6% ΔV of melting at the Martian CMB that decreases at greater depth. We have also investigated the effect of imposing fixed ΔV values from 2–5%. This range corresponds to a change in core radius of 56 km.

One of the geophysical constraints on the Martian interior comes from its deformation in response to tidal forcings from the Sun, Phobos, and Deimos. The tidal Love number k_2 has been determined from spacecraft and lander tracking data, most recently in Konopliv et al. (2016), which reported a value of 0.169 ± 0.006. To evaluate the consistency between this value and our profiles of the Martian interior, we used a simplified two-layer parameterization for calculating k_2 (see supplementary materials for more details). The dissipation of tidal energy within Mars is dependent on the rigidity of the core and mantle layers and their relative sizes. A liquid core cannot sustain shear stress, so its rigidity is negligible; therefore, a very rigid mantle requires a large core to match the planetary k_2. This tradeoff indicates that, for example, a mean mantle rigidity of μ = 80 GPa requires a core 1840–1900 km in radius to match k_2, while a softer mantle with μ = 60 GPa only requires a 1540–1640 km core (Supplementary Figure S3). If the Martian mantle accurately reflects the volumetrically averaged shear modulus of ~73 GPa calculated here, then the core should be 1740–1820 km in radius. It is possible to produce a core of at least this size through several combinations of the parameters considered above, even accounting for the constraint on crust size from MOI. The relationship between core radius and the geophysical and geochemical parameters considered here is illustrated in Figures 7 and S4, and can be parameterized by the following equation:

$$R_{core} = 564 + 1.49\ d_{crust} + 10.1\ C^{S}_{core} + 0.183(C^{S}_{core})^2 + 0.115\ \Delta T_{TBL}$$
$$+0.000108\ (\Delta T_{TBL})^2 + 0.423\ T_P + 14.8\ \Delta V_{core} + 0.337\ (\Delta V_{core})^2 \quad (1)$$

where R_{core} is the radius of the core (km), d_{crust} is the thickness of the crust (km), C^{S}_{core} is the S content of the core (wt%), ΔT_{TBL} is the temperature contrast across the core–mantle thermal boundary layer (K), T_P is the mantle potential temperature (K), and ΔV_{core} is the volume change of melting associated with the core alloy (%; e.g., for a 2% volume change of melting, ΔV_{core} = 2). This equation reproduces the results of our geophysical model with a root mean squared misfit of 9 km for core radii of 1450–2000 km and the parameter ranges listed above and should not be applied to more extreme cases. Future seismological constraints on crust thickness and core radius can be inserted into this equation to help constrain geophysical properties of the Martian interior.

It is also possible that the Martian mantle is less rigid than the melt-free anhydrous idealization depicted here and by other studies. Shear moduli are significantly reduced by both the presence of H and partial melts in mantle minerals. The 300 ppm water suggested to reside in the Martian mantle (Taylor, 2013) would not significantly reduce the mean shear modulus, but Martian water abundances are extremely uncertain. Partial melting is another possibility; fluids cannot support shear stress, so partial melts would decrease the mean shear modulus by the same amount as their volume fraction. Selecting a crust size of 55 km, a potential temperature of 1600 K, a core S content of 18 wt%, no TBL, and ΔV of melting of 3% returns a core 1620 km in radius. To match k_2, this core would require a mean mantle rigidity of 55 GPa, a 15% reduction from our nominal value. This amounts to a basal magma ocean 500 km deep. Such a feature is unlikely, but volumetrically significant melting may also occur beneath the Martian lithosphere (Duncan et al., 2018). Ultimately, some combination of mantle-softening and core-expanding parameters must be responsible for the observed Martian k_2.

4.5 Density and velocity profiles of the Martian interior

We consider the effects of the same five geochemical and geophysical parameters (crust thickness, core and mantle T, core S content, Fe–S ΔV of melting) on the density and velocity structure of the Martian interior (Figure 4). Unlike some previously-modeled velocity profiles (e.g., Khan and Connolly, 2008; Zharkov and Gudkova, 2009), we predict a low-velocity zone in the upper mantle due to the steep lithospheric temperature gradient (Section 4.1). Our results share many properties in common with previous LVZ models, such as the large contrast between adiabatic and lithospheric temperatures (Nimmo and Faul, 2013) and a gradual olivine–

wadsleyite phase transition due to the high FeO content. This study predicts a V_S in the lowermost mantle that is smaller than V_P at the top of the core, whereas the otherwise similar LVZ model of Zheng et al. (2015) does not (Figure 5). The lower V_P of Zheng et al. (2015) is likely due to their use of FeS data for the thermophysical properties of the core alloy; FeS has a reduced density and bulk modulus compared to our more moderate composition.

4.6 Seismic properties

Mode center frequencies for the suite of models have been calculated (Figure 8a and S5). Overall, as expected, radial, core-sensitive, and Stonely modes are affected by adjusting the five parameters described above. Stonely modes are confined to the CMB and are very challenging to observe even on Earth. Modes with center frequencies below 5 mHz are unlikely to be detectable on Mars (Panning et al., 2017), but radial modes (on the left of Figure 8a) above this period may display changes in frequency of several percent. While not affected by the physical properties of the core itself, we note that models with different crustal thicknesses and mantle potential temperatures will result in different frequencies for the fundamental modes, which are a target for observation (Bissig et al., 2018). Thus, any observations of normal modes on Mars will aid in discrimination between these different models of Martian formation.

Body wave travel times (Figure 8b) show that a range of phases that are reflected at the CMB or travel through the core are sensitive to the parameters explored here. As all the models investigated have an LVZ in the upper mantle (Section 4.1), shadow zones are evident in the travel time curves, most prominently in the direct S phase. Models with larger cores show earlier arriving core-reflected phases (for example ScS), whilst signals like PKP are delayed as V_P in the core is lower than that of the mantle. SKS, which travels through the mantle as a shear wave and through the liquid core as a compressional wave, has delay times that vary little though the model suite as V_s in the mantle is very close to V_P in the core. If it can be observed, SKKS, which transits the core twice, would be a better indicator of core size; SKKS's amplitude may be insufficient to observe in InSight data however. Because V_P just below the CMB is higher than V_S just above the CMB in our models, we predict the presence of minor arc SKKS at a wide range of distances (Helffrich, 2017).

The InSight site is roughly 20° from Cerberus Fossae (Taylor et al., 2013). At such a distance, one of the clearest core signals we hope to observe will be ScS. Figure 9 shows predicted travel times for this phase at this epicentral distance for the full suite of core models. Nearly all the parameters behave in the same way: shorter ScS travel times correspond to larger core radii. Thus, even though all properties may not be discernable from such an observation, a travel time should permit us to roughly estimate core radius in this framework. Mantle potential temperature has effects on the radius–ScS time relationship which are not co-linear with the other parameters because a hotter potential temperature both decreases mantle velocities and changes core radius. Both crustal thickness and mantle potential temperature may be obtainable from other seismological observables (e.g., receiver function analysis for the former, and estimates of the sub-lithospheric LVZ for the latter), making this kind of analysis more valuable as the possible parameter space is narrowed down further.

5. Conclusions

A multi-stage core formation model has successfully reproduced meteorite-based compositions of the bulk silicate Mars and has been used to determine conditions of core formation and the composition of the Martian core. The high FeO content of the Martian mantle relative to that of Earth is due to formation from primordial material initially equilibrated at approximately IW–1.25. On average, >85% of incoming metal was equilibrated with >30% of the Martian mantle upon impact, and equilibration took place at a depth of 45–91% of the evolving CMB pressure. The light element composition of the Martian core is dominated by S (16–20 wt%), with <1 wt% O and negligible Si.

We have considered the possible ranges of various geophysical parameters (mantle and core temperatures, crustal thickness, and density of the Fe–S core alloy) and evaluated the effects of varying these parameters on the structure of the Martian interior. The core alloy densities calculated here are somewhat higher than those of previous studies due to different interpretations of the Fe–S equation of state data. Conservative parameter combinations imply that the core could be as small as 1620 km, though this size is not consistent with geophysical constraints on tidal Love number k_2 unless the Martian mantle is significantly softened by the presence of melt or water. Larger values of the crustal thickness, mantle temperature, core temperature, or S content imply larger cores (Equation 1). If the Martian mantle is not subject to any softening effects, the core can be as large as 1820 km while maintaining consistency with geophysical observations. We have calculated seismic phase arrival times and planetary normal modes for a variety of parameter combinations to facilitate comparison with InSight's upcoming seismological measurements. Whatever the results of these observations, the actual core radius implies a particular combination of geophysical and geochemical parameters, meaning that constraints on core radius will help elucidate the thermal, physical, and compositional state of the Martian interior.

Acknowledgements

This work was supported by NASA grants NNX17AE27G and 80NSSC18K1633 and National Science Foundation grants 1644399 and 1736046. We thank Yingcai Zheng and Tamara

Gudkova for providing their models for comparison, and Francis Nimmo, Roger Fu, and Junjie Dong for their helpful advice.

Figures

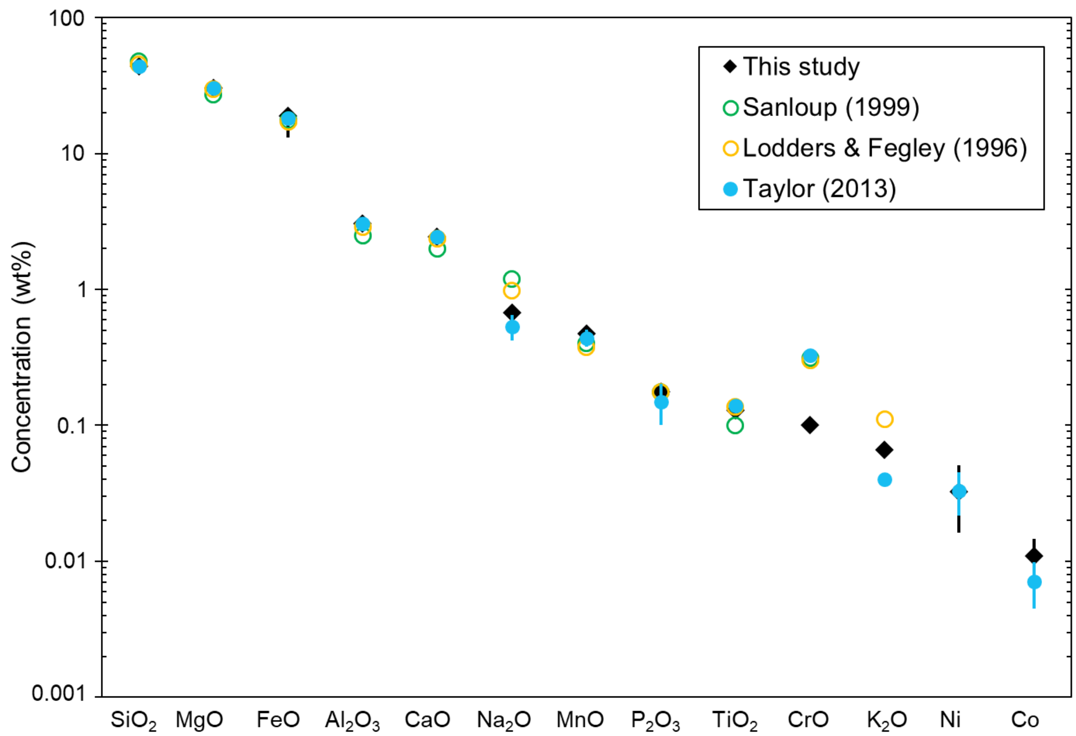

Fig. 1. Comparison of bulk mantle compositions between this study and models based on SNC elemental abundances (Taylor, 2013) or O isotopes (Lodders and Fegley, 1996; Sanloup, 1999). Error bars correspond to 95% confidence intervals of our Monte Carlo analysis for this study and reported 2σ uncertainties for Taylor (2013). Calculation was performed for $k = 0.9$, whole mantle equilibration, $P_{equil}/P_{CMB} = 0.66$, and initial fO_2 of IW–1.2.

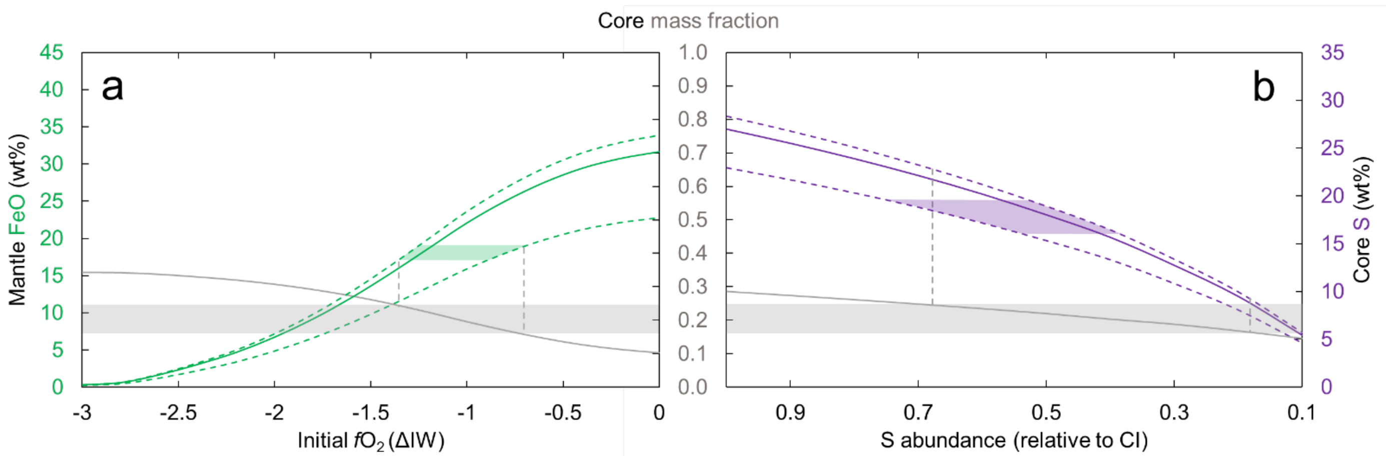

Fig. 2. a. The tradeoff between the initial fO_2 of Mars' primordial material and the partitioning of Fe between mantle and core. The green shaded region indicates the range of calculated FeO contents that are consistent with Taylor (2013), which constrain the initial fO_2 to be IW–0.7 to IW–1.4. The corresponding core mass fraction is 0.17–0.26 (grey curve and grey horizontal shaded bar). **b.** The tradeoff between bulk S content and S content of the core (purple). For the same range of core mass fractions as in **a** (grey curve and grey horizontal shaded bar), the total S content of bulk Mars is constrained to be 0.20–0.68 × CI. The purple shaded region represents the range of core S contents from the core formation model. Dashed lines represent 95% confidence intervals at P_{equil}/P_{CMB} = 0.66 and k = 0.9.

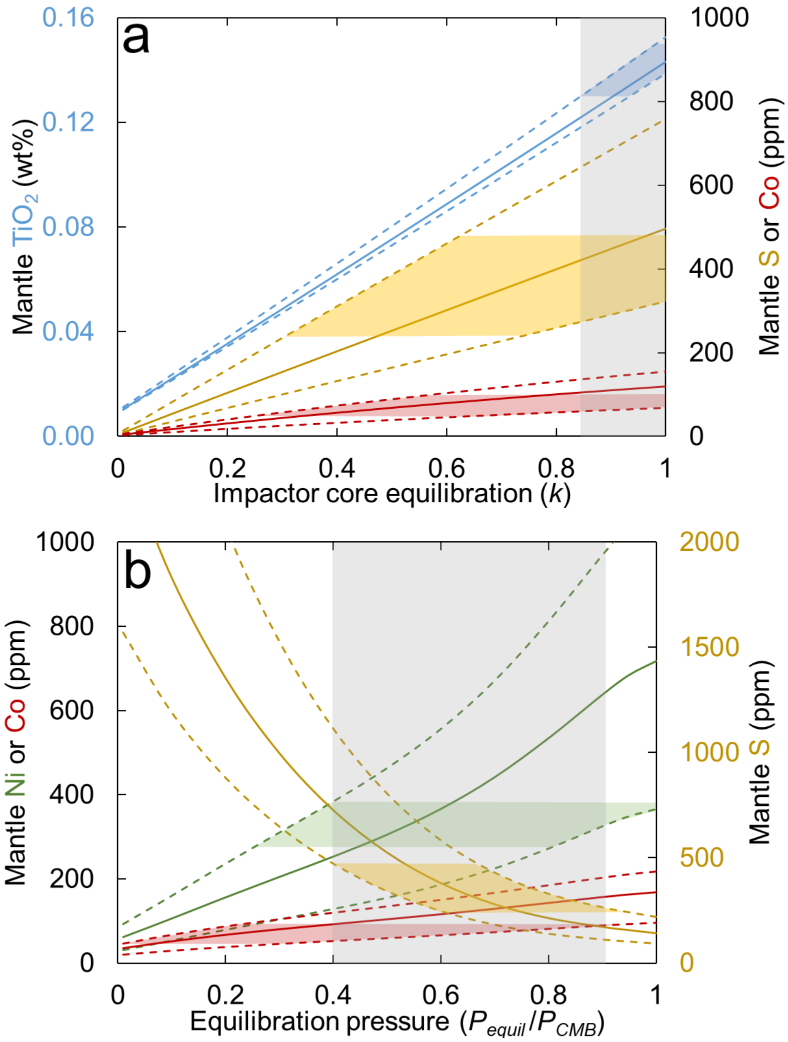

Fig. 3. a. Variation in the mantle concentrations of TiO_2 (blue), Co (red), and S (yellow) as a function of the degree of impactor core equilibration, *k*. Dashed lines are 95% confidence intervals. The colored regions illustrate where the calculated compositions are consistent with the previously published values of Taylor (2013) for TiO_2 and Co, and Wang and Becker (2017) for S. The grey shaded bar indicates the range of *k* in which all three elements can be matched. These values of *k* suggest that most metal was emulsified and equilibrated before merging with the Martian core. Calculation was performed for whole mantle equilibration, P_{equil}/P_{CMB} = 0.66, and initial fO_2 of IW–1.2. **b.** Variations in the mantle concentrations of Ni (green), Co (red), and S (yellow) as a function of core–mantle equilibration pressure (expressed as a fraction of the evolving CMB pressure). The colored regions illustrate where the calculated compositions are consistent with the previously published values of Taylor (2013) for Ni and Co and Wang, and Becker (2017) for S. These values of equilibration pressure suggest that equilibration occurred in a deep magma ocean, but not at the core–mantle boundary. Calculation was performed for *k* = 0.9, whole mantle equilibration, and initial fO_2 of IW–1.2.

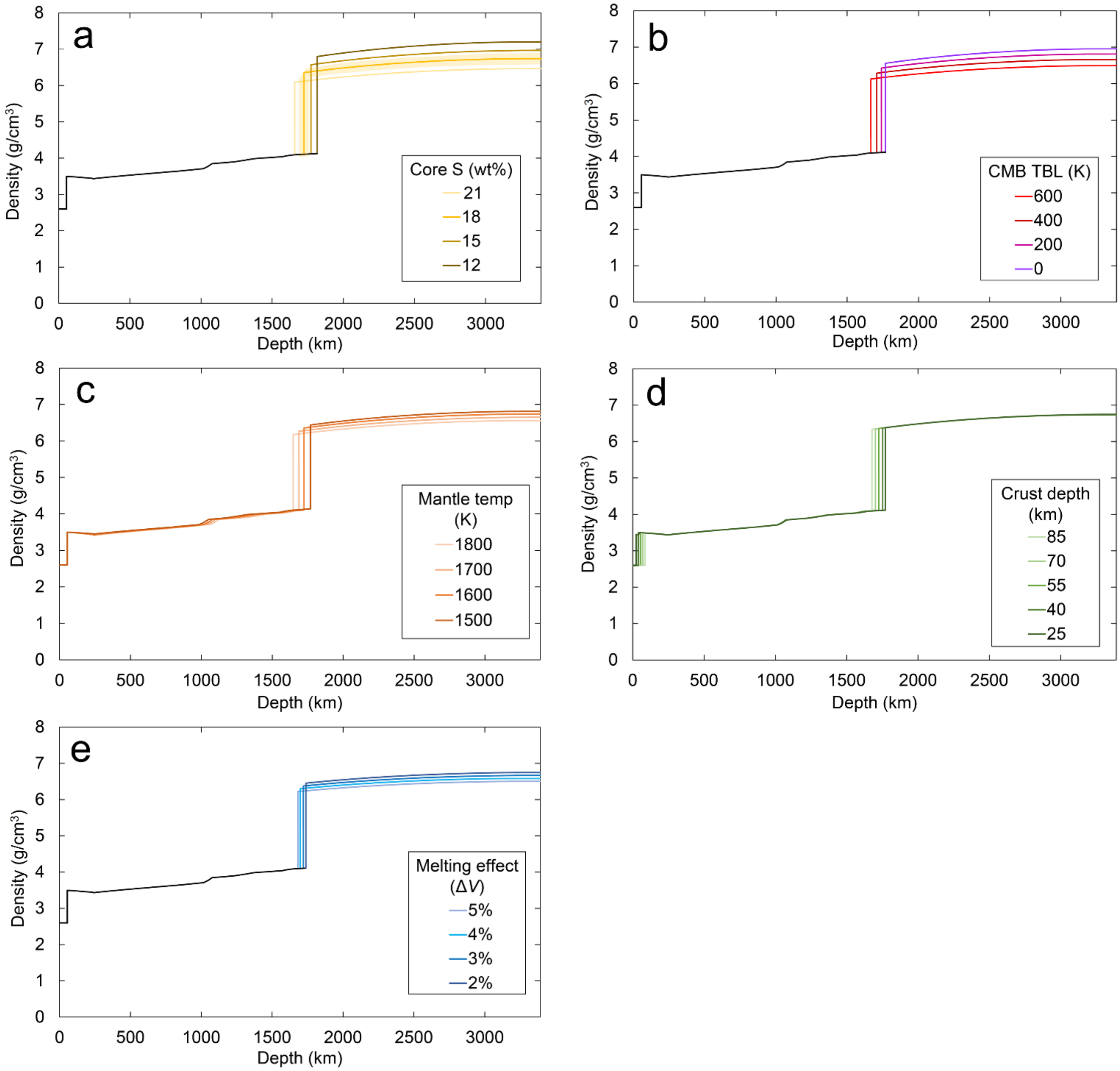

Fig. 4. Martian density profiles calculated by varying a single parameter at a time: core S content (**a**), temperature contrast between the lowermost mantle and uppermost core (assuming a thin thermal boundary layer at the CMB) (**b**), mantle potential temperature (**c**), crustal thickness (**d**), and ΔV of melting of Fe–S alloys (**e**). The shaded region in (**a**) corresponds to our preferred S range of 16–20 wt% from the core formation model at initial fO_2 = IW–1.2, $P_{equil}/P_{CMB} = 0.66$ and $k = 0.9$ (Section 3.2).

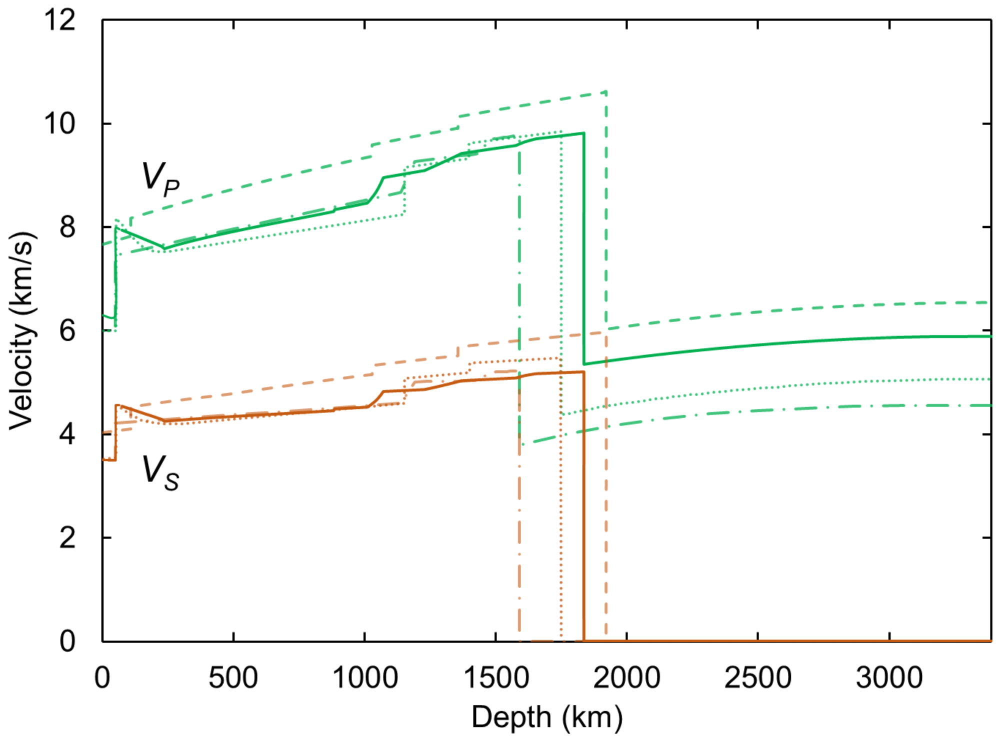

Fig. 5. Comparison of Martian compressional wave velocity (V_P) and shear wave velocity (V_S) profiles between this and several previous studies (dashed line: Sohl and Spohn, 1997 "Model A"; dotted line: Zheng et al., 2015 "LVZ Model"; dot-dashed line: Zharkov and Gudkova, 2009 "M14_3 Model"). The profile for this study corresponds to a core sulfur content of 18 wt%, crustal thickness of 50 km, thermal boundary layer temperature contrast of 300 K, and mantle potential temperature of 1600 K. The low-velocity zone in the upper mantle is a consequence of the steep lithospheric temperature profile within the stagnant lid on Mars (Section 4.1).

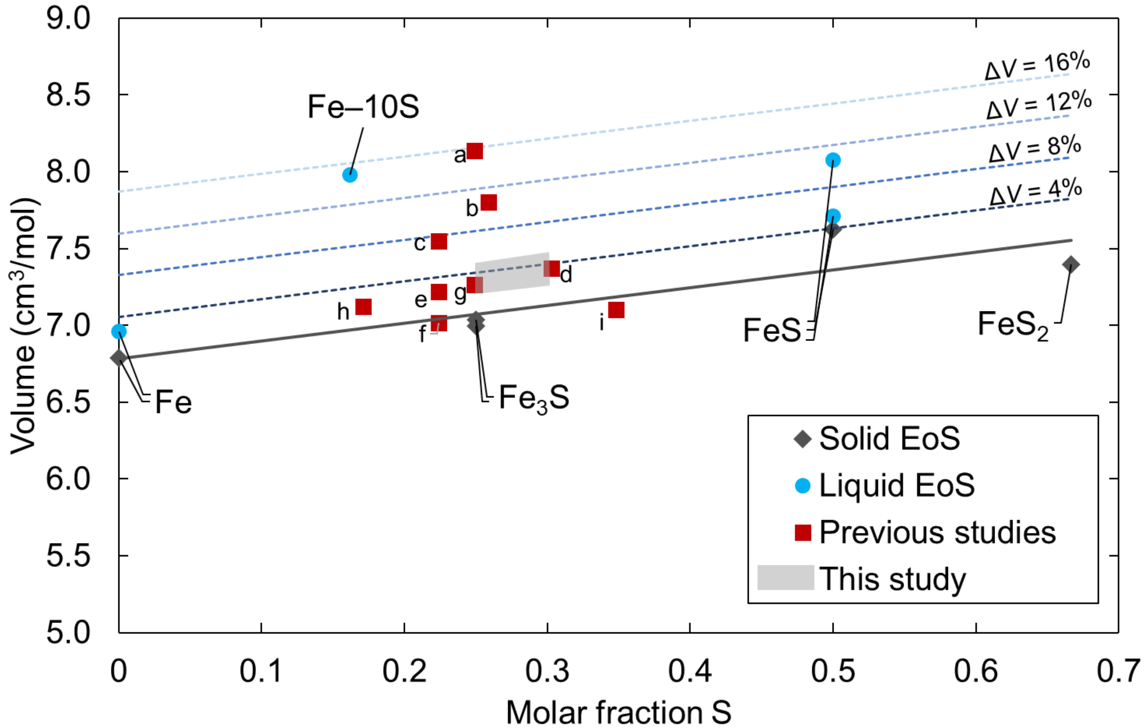

Fig. 6. Densities of solid (Chen et al., 2008; Kombayashi et al., 2010; Seagle et al., 2006; Thompson et al., 2016; Urakawa et al., 2004) and liquid (Anderson and Ahrens, 1994; Balog et al., 2003; Morard et al., 2018; Nishida et al., 2011) alloys in the Fe–S system calculated from equations of state at 20 GPa and 2000 K. The solid line is a linear fit to the solid data, and the dashed lines are offset from this line according to fixed ΔV of melting up to the 1 bar ΔV of FeS (Kaiura and Toguri, 1979). The grey box indicates the range of S contents within uncertainty of the core formation model and the range of ΔV between that of Fe and FeS at these conditions. All liquid equations of state have been extrapolated beyond the pressure conditions of the original measurements, save for the Fe–10S study (Balog et al., 2003) which was based on sink/float experiments with large (~20%) error bars. Using this data point to derive the properties of the Fe–S alloy (Khan et al., 2018; Rivoldini et al., 2011) results in an implied ΔV greater than that of FeS at 1 bar, which is physically unlikely. Red squares represent some previous models of the Martian core alloy (**a**: Rivoldini et al., 2011; **b**: Khan et al., 2018; **c**: Sohl and Spohn, 1997; **d**: Zharkov and Gudkova, 2005; **e**: Kavner et al., 2001; **f**: Bertka and Fei, 1998; **g**: Sanloup, 1999; **h**: Lodders and Fegley, 1997; **i**: Khan and Connolly, 2008). Studies **a**–**f** are plotted at the same P–T conditions as the equation of state points, while studies **g**–**i** have fixed (P–T independent) core densities.

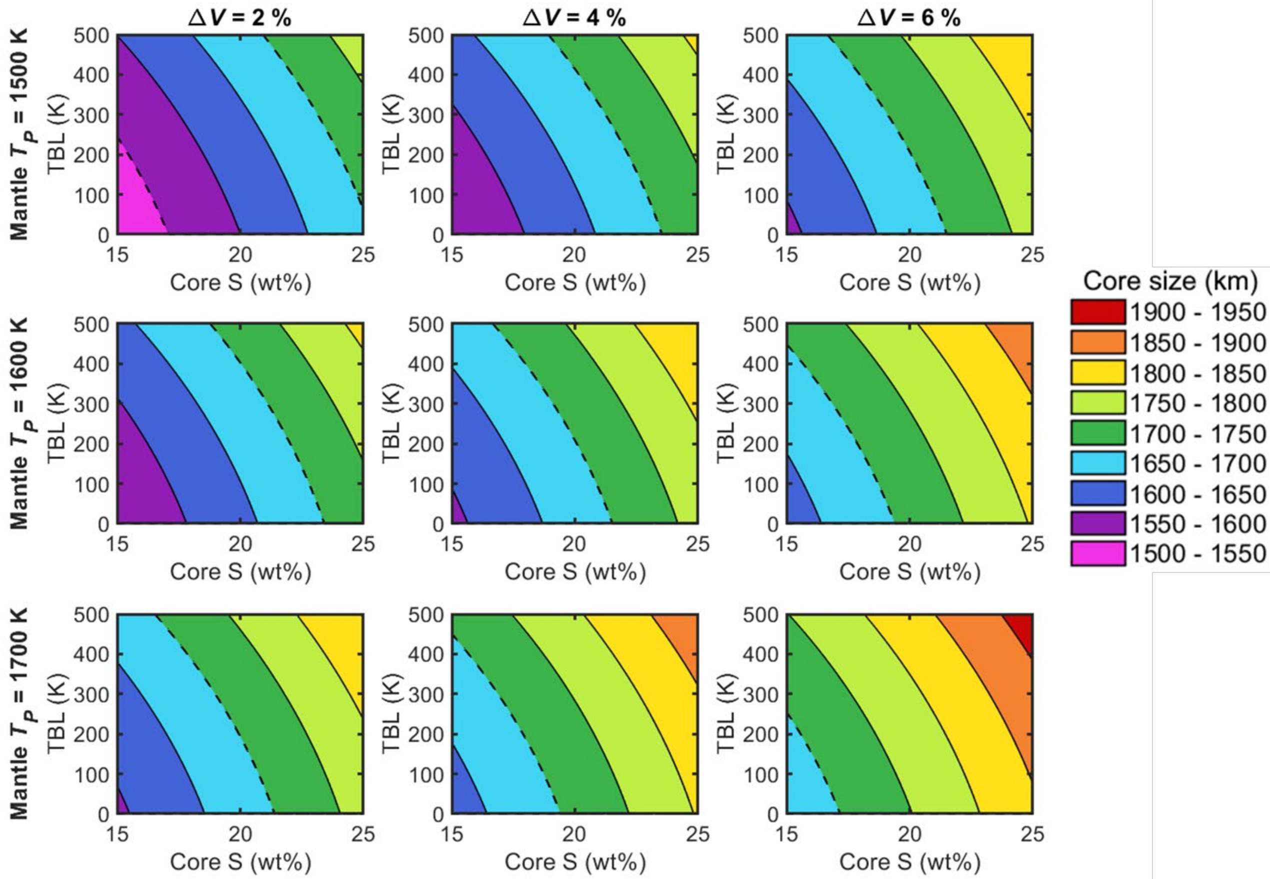

Fig 7. Tradeoffs between parameters that influence core size as parameterized by Equation 1. Each panel represents a fixed combination of *ΔV* of melting (constant throughout each column) and mantle potential temperature (constant throughout each row) and shows the combinations of core S content and CMB thermal boundary layer temperature contrast that can produce cores of a certain size. Each contour connects cores of the same radius. All plots correspond to a 55 km crust. For this crust size, the approximate MOI constraints on core size (1550–1700 km) are indicated by dashed lines. Supplementary Figure S4 shows alternate versions of this figure corresponding to different crustal thicknesses.

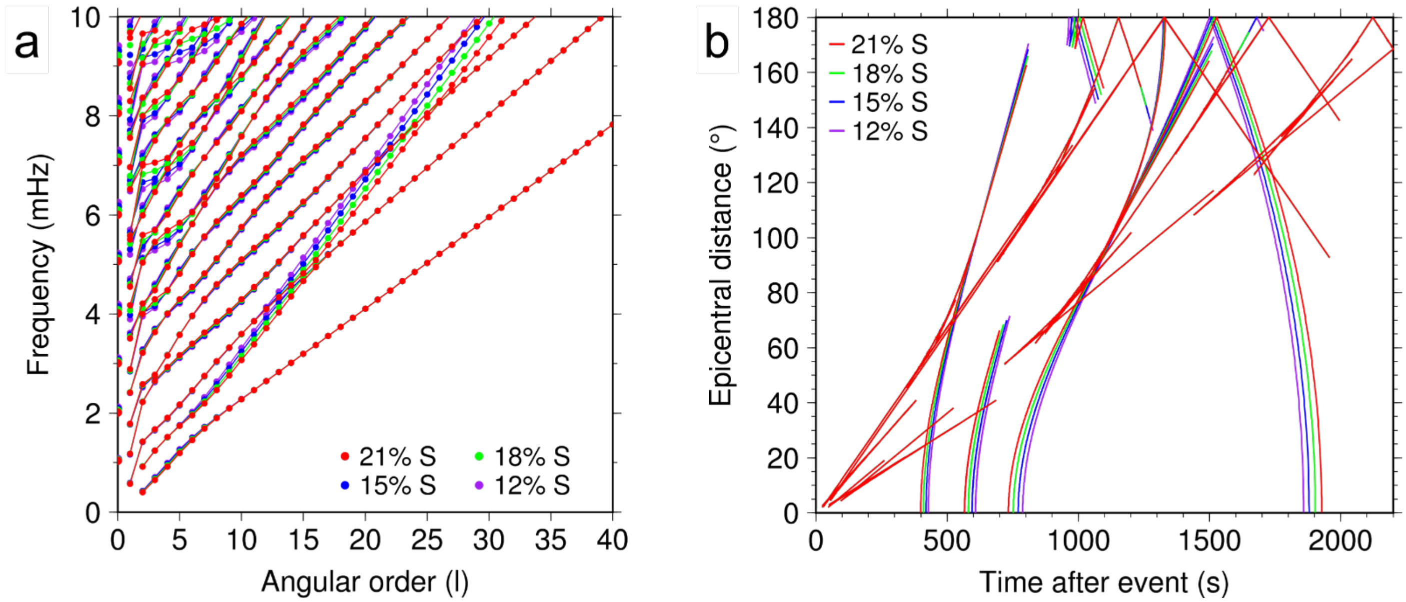

Fig. 8. Seismological observables corresponding to four models with different core S contents. **a.** Normal mode center frequencies. The radial modes sit on the vertical axis (l=0). InSight's broadband seismometer is expected to be unable to detect those modes under 5 mHz. **b.** Body wave travel time predictions for a 5 km deep marsquake. Seismic phases P, PP, PcP, P_{diff}, S, SS, ScS, S_{diff}, PcS, ScP, SP, PKP, SKS, and SKKS are shown.

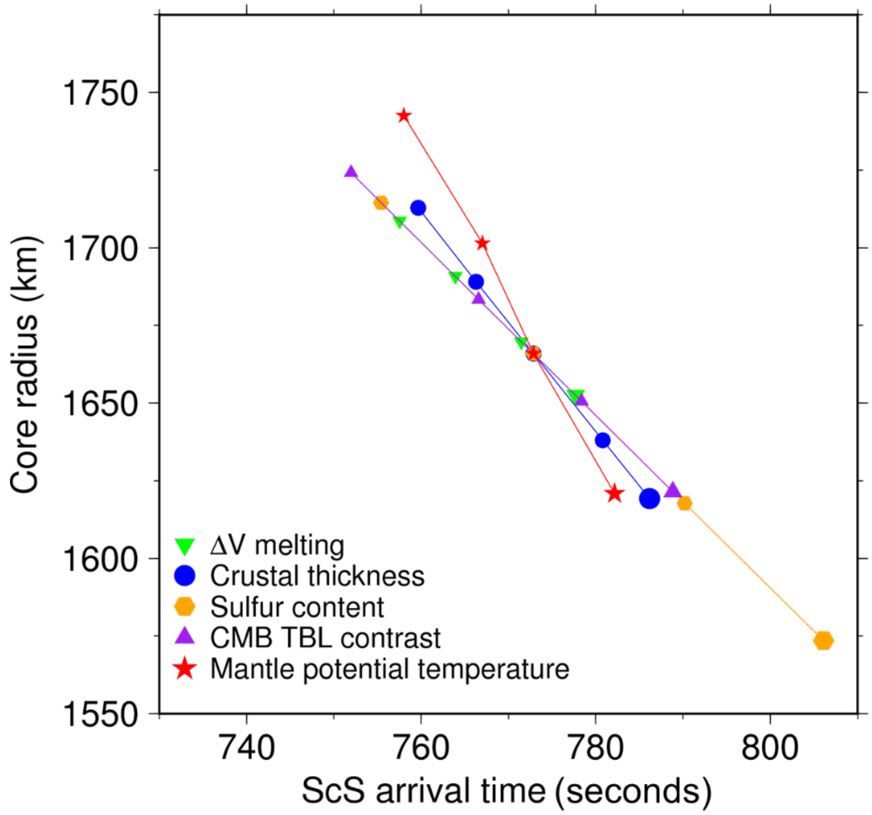

Fig. 9. Relationship between core radius and predicted ScS arrival time. Travel times are predicted for an epicentral distance of 20° and a marsquake depth of 5 km. The impact of each of the five parameters on core radius is discussed in Section 4.4. In each case the larger symbol corresponds to the lowest value of the parameter that is being varied.

Appendix A. Supplementary materials

References

Anderson, D.L., 1972. Internal constitution of Mars. Journal of Geophysical Research 77, 789-795.

Anderson, W.W., Ahrens, T.J., 1994. An equation of state for liquid iron and implications for the Earth's core. Journal of Geophysical Research: Solid Earth 99, 4273-4284.

Balog, P., Secco, R., Rubie, D., Frost, D., 2003. Equation of state of liquid Fe-10 wt% S: Implications for the metallic cores of planetary bodies. Journal of Geophysical Research: Solid Earth 108, 2124, B2.

Bertka, C.M., Fei, Y., 1997. Mineralogy of the Martian interior up to core-mantle boundary pressures. Journal of Geophysical Research: Solid Earth 102, 5251-5264.

Bertka, C.M., Fei, Y., 1998. Implications of Mars Pathfinder Data for the Accretion History of the Terrestrial Planets. Science 281, 1838-1840.

Bissig, F., Khan, A., Van Driel, M., Stähler, S.C., Giardini, D., Panning, M., Drilleau, M., Lognonné, P., Gudkova, T.V., Zharkov, V.N., 2018. On the detectability and use of normal modes for determining interior structure of Mars. Space Science Reviews 214, 114.

Breuer, D., Yuen, D.A., Spohn, T., Zhang, S., 1998. Three dimensional models of Martian mantle convection with phase transitions. Geophysical Research Letters 25, 229-232.

Campbell, A.J., Seagle, C.T., Heinz, D.L., Shen, G., Prakapenka, V., 2008. Partial melting in the iron–sulfur system at high pressure: A synchrotron X-ray diffraction study. Physics of the Earth and Planetary Interiors 162, 119-128.

Chen, B., Gao, L., Funakoshi, K.-i., Li, J., 2007. Thermal expansion of iron-rich alloys and implications for the Earth's core. Proceedings of the National Academy of Sciences 104, 9162-9167.

Chi, H., Dasgupta, R., Duncan, M.S., Shimizu, N., 2014. Partitioning of carbon between Fe-rich alloy melt and silicate melt in a magma ocean – Implications for the abundance and origin of volatiles in Earth, Mars, and the Moon. Geochimica et Cosmochimica Acta 139, 447-471.

Clesi, V., Bouhifd, M.A., Bolfan-Casanova, N., Manthilake, G., Schiavi, F., Raepsaet, C., Bureau, H., Khodja, H., Andrault, D., 2018. Low hydrogen contents in the cores of terrestrial planets. Science Advances 4, e1701876.

Dreibus, G., Wanke, H., 1985. Mars, a volatile-rich planet. Meteoritics 20, 367-381.

Duncan, M.S., Schmerr, N.C., Bertka, C.M., Fei, Y., 2018. Extending the Solidus for a Model Iron-Rich Martian Mantle Composition to 25 GPa. Geophysical Research Letters 45, 10211-10220.

Fei, Y., Van Orman, J., Li, J., Van Westrenen, W., Sanloup, C., Minarik, W., Hirose, K., Komabayashi, T., Walter, M., Funakoshi, K., 2004. Experimentally determined postspinel transformation boundary in Mg_2SiO_4 using MgO as an internal pressure standard and its geophysical implications. Journal of Geophysical Research: Solid Earth 109, B02305.

Fischer, R.A., Campbell, A.J., Ciesla, F.J., 2017. Sensitivities of Earth's core and mantle compositions to accretion and differentiation processes. Earth and Planetary Science Letters 458, 252-262.

Fischer, R.A., Nakajima, Y., Campbell, A.J., Frost, D.J., Harries, D., Langenhorst, F., Miyajima, N., Pollok, K., Rubie, D.C., 2015. High pressure metal–silicate partitioning of Ni, Co, V, Cr, Si, and O. Geochimica et Cosmochimica Acta 167, 177-194.

Fischer, R.A., Nimmo, F., 2018. Effects of core formation on the Hf–W isotopic composition of the Earth and dating of the Moon-forming impact. Earth and Planetary Science Letters 499, 257-265.

Grott, M., Baratoux, D., Hauber, E., Sautter, V., Mustard, J., Gasnault, O., Ruff, S.W., Karato, S.-I., Debaille, V., Knapmeyer, M., 2013. Long-term evolution of the Martian crust-mantle system. Space Science Reviews 174, 49-111.

Helffrich, G., 2017. Mars core structure—concise review and anticipated insights from InSight. Progress in Earth and Planetary Science 4, 24.

Kaiura, G.H., Toguri, J.M., 1979. Densities of the Molten Fes, FeS–Cu_2S and Fe–S–O Systems—Utilizing A Bottom-Balance Archimedean Technique. Canadian Metallurgical Quarterly 18, 155-164.

Kavner, A., Duffy, T.S., Shen, G., 2001. Phase stability and density of FeS at high pressures and temperatures: implications for the interior structure of Mars. Earth and Planetary Science Letters 185, 25-33.

Khan, A., Connolly, J.A.D., 2008. Constraining the composition and thermal state of Mars from inversion of geophysical data. Journal of Geophysical Research: Planets 113, E07003.

Khan, A., Liebske, C., Rozel, A., Rivoldini, A., Nimmo, F., Connolly, J., Plesa, A.C., Giardini, D., 2018. A geophysical perspective on the bulk composition of Mars. Journal of Geophysical Research: Planets 123, 575-611.

Komabayashi, T., Fei, Y., 2010. Internally consistent thermodynamic database for iron to the Earth's core conditions. Journal of Geophysical Research: Solid Earth 115, B03202.

Konopliv, A.S., Asmar, S.W., Folkner, W.M., Karatekin, Ö., Nunes, D.C., Smrekar, S.E., Yoder, C.F., Zuber, M.T., 2011. Mars high resolution gravity fields from MRO, Mars seasonal gravity, and other dynamical parameters. Icarus 211, 401-428.

Konopliv, A.S., Park, R.S., Folkner, W.M., 2016. An improved JPL Mars gravity field and orientation from Mars orbiter and lander tracking data. Icarus 274, 253-260.

Lodders, K., Fegley, B., 1997. An Oxygen Isotope Model for the Composition of Mars. Icarus 126, 373-394.

Lodders, K., Fegley, B., 1998. The planetary scientist's companion. Oxford University Press.

Michel, N., Forni, O., 2011. Mars mantle convection: Influence of phase transitions with core cooling. Planetary and Space Science 59, 741-748.

Morard, G., Bouchet, J., Rivoldini, A., Antonangeli, D., Roberge, M., Boulard, E., Denoeud, A., Mezouar, M., 2018. Liquid properties in the Fe-FeS system under moderate pressure: Tool box to model small planetary cores. American Mineralogist 103, 1770-1779.

Nimmo, F., Faul, U.H., 2013. Dissipation at tidal and seismic frequencies in a melt-free, anhydrous Mars. Journal of Geophysical Research: Planets 118, 2558-2569.

Nishida, K., Ohtani, E., Urakawa, S., Suzuki, A., Sakamaki, T., Terasaki, H., Katayama, Y., 2011. Density measurement of liquid FeS at high pressures using synchrotron X-ray absorption. The American Mineralogist 96, 864.

Panning, M., Lognonné, P., Bruce Banerdt, W., Garcia, R., Golombek, M., Kedar, S., Knapmeyer-Endrun, B., Mocquet, A., Teanby, N., Tromp, J., Weber, R., Beucler, E., Blanchette-Guertin, J.-F., Bozdağ, E., Drilleau, M., Gudkova, T., Hempel, S., Khan, A., Lekić, V., Murdoch, N., Plesa, A.-C., Rivoldini, A., Schmerr, N., Ruan, Y., Verhoeven, O., Gao, C., Christensen, U., Clinton, J., Dehant, V., Giardini, D., Mimoun, D., Thomas Pike, W., Smrekar, S., Wieczorek, M., Knapmeyer, M., Wookey, J., 2017. Planned Products of the Mars Structure Service for the InSight Mission to Mars. Space Science Reviews 211, 611-650.

Rai, N., van Westrenen, W., 2013. Core-mantle differentiation in Mars. Journal of Geophysical Research. Planets, 1195-1203.

Righter, K., Chabot, N., 2011. Moderately and slightly siderophile element constraints on the depth and extent of melting in early Mars. Meteoritics and Planetary Science 46, 157-176.

Rivoldini, A., Van Hoolst, T., Verhoeven, O., Mocquet, A., Dehant, V., 2011. Geodesy constraints on the interior structure and composition of Mars. Icarus 213, 451-472.

Rubie, D., Frost, D., Mann, U., Asahara, Y., Nimmo, F., Tsuno, K., Kegler, P., Holzheid, A., Palme, H., 2011. Heterogeneous accretion, composition and core-mantle differentiation of the Earth. Earth and Planetary Science Letters 301, 31-42.

Rubie, D.C., Jacobson, S.A., Morbidelli, A., O'Brien, D.P., Young, E.D., de Vries, J., Nimmo, F., Palme, H., Frost, D.J., 2015. Accretion and differentiation of the terrestrial planets with implications for the compositions of early-formed Solar System bodies and accretion of water. Icarus 248, 89-108.

Sanloup, C., Jambon, A., Gillet, P., 1999. A simple chondritic model of Mars. Physics of the Earth and Planetary Interiors 112, 43-54.

Seagle, C.T., Campbell, A.J., Heinz, D.L., Shen, G., Prakapenka, V.B., 2006. Thermal equation of state of Fe_3S and implications for sulfur in Earth's core. Journal of Geophysical Research: Solid Earth 111, B06209.

Sohl, F., Spohn, T., 1997. The interior structure of Mars: Implications from SNC meteorites. Journal of Geophysical Research: Planets 102, 1613-1635.

Steenstra, E.S., van Westrenen, W., 2018. A synthesis of geochemical constraints on the inventory of light elements in the core of Mars. Icarus 315, 69-78.

Taylor, G.J., 2013. The bulk composition of Mars. Chemie der Erde 73, 401-420.

Taylor, J., Teanby, N., Wookey, J., 2013. Estimates of seismic activity in the Cerberus Fossae region of Mars. Journal of Geophysical Research: Planets 118, 2570-2581.

Thompson, E.C., Chidester, B.A., Fischer, R.A., Myers, G.I., Heinz, D.L., Prakapenka, V.B., Campbell, A.J., 2016. Equation of state of pyrite to 80 GPa and 2400 K. American Mineralogist 101.

Tsuno, K., Grewal, D.S., Dasgupta, R., 2018. Core-mantle fractionation of carbon in Earth and Mars: The effects of sulfur. Geochimica et Cosmochimica Acta 238, 477-495.

Urakawa, S., Someya, K., Terasaki, H., Katsura, T., Yokoshi, S., Funakoshi, K.-I., Utsumi, W., Katayama, Y., Sueda, Y.-I., Irifune, T., 2004. Phase relationships and equations of state for FeS at high pressures and temperatures and implications for the internal structure of Mars. Physics of the Earth and Planetary Interiors 143, 469-479.

Wang, Z., Becker, H., 2017. Chalcophile elements in Martian meteorites indicate low sulfur content in the Martian interior and a volatile element-depleted late veneer. Earth and Planetary Science Letters 463, 56-68.

Wanke, H., Dreibus, G., 1988. Chemical Composition and Accretion History of Terrestrial Planets. Philosophical Transactions of the Royal Society of London. Series A, Mathematical and Physical Sciences 325, 545-557.

Wieczorek, M.A., Zuber, M.T., 2004. Thickness of the Martian crust: Improved constraints from geoid-to-topography ratios. Journal of Geophysical Research: Planets 109, E01009.
Williams, J.-P., Nimmo, F., 2004. Thermal evolution of the Martian core: Implications for an early dynamo. Geology 32, 97-100.
Zharkov, V., Gudkova, T., 2005. Construction of Martian Interior Model. Solar System Research 39, 343-373.
Zharkov, V., Gudkova, T., Molodensky, S., 2009. On models of Mars' interior and amplitudes of forced nutations: 1. the effects of deviation of Mars from its equilibrium state on the flattening of the core–mantle boundary. Physics of the Earth and Planetary Interiors 172, 324-334.
Zheng, Y., Nimmo, F., Lay, T., 2015. Seismological implications of a lithospheric low seismic velocity zone in Mars. Physics of the Earth and Planetary Interiors 240, 132-141.